

Fluid Motion Planner for Nonholonomic 3-D Mobile Robots With Kinematic Constraints

Darwin Lau, Jonathan Eden, and Denny Oetomo

Abstract—Fluid motion planners are a type of artificial potential field (APF) motion planners that use the differential equations of fluid flow to determine the desired trajectory. The fluid flow approach in motion planning can efficiently produce natural-looking trajectories. However, the differential equations used in previous studies are restricted to motion planning in 2-D environments. In this paper, the fluid flow approach is extended to a motion planning framework for 3-D mobile robots that avoids spheroidal obstacles. Compared with existing APF approaches, kinematic constraints in both speed and curvature are also considered. Possessing the efficiency of 2-D fluid motion planners, the proposed approach is able to plan natural-looking reference trajectories for nonholonomic 3-D mobile robots. The approach is demonstrated through various 3-D example scenarios. The work can be considered as a fundamental framework for 3-D fluid motion planning, where additional kinematic constraints and more complex scenarios can be incorporated.

Index Terms—Artificial Potential Field, Mobile Robots, Nonholonomic Motion Planning, 3-D Motion Planning.

I. INTRODUCTION

Motion planning of mobile robots has been heavily researched and used in a range of environments: from structured factory floors to completely unstructured environments, such as disaster sites. In recent years, the challenging problem of motion planning in 3-D environments has attracted attention. Key challenges in 3-D motion planning include obstacle avoidance [1]–[4], computational efficiency for real-time implementation, smooth navigation within dynamic environments, and the consideration of kinematic constraints. Kinematic constraints such as maximum speed, minimum radius of curvature, and non-holonomicity are important for 3-D mobile robots, such as fixed-wing unmanned aerial vehicles (UAVs) [5], [6], due to its physical and actuator limitations.

Many techniques have been investigated for motion planning within 3-D environments. *Search* methods [7]–[10] generate a trajectory by performing a search within a discretized representation of the environment. The major drawback of search

methods is that the time complexity typically increases significantly with the resolution of the search space discretization and the incorporation of kinematic constraints. *Spline* methods [1], [11], [12] use geometric splines that satisfy the desired constraints to represent the resulting trajectory. Obstacle avoidance can be achieved by specifying intermediate goal locations. However, spline approaches may get stuck in complex environments. *Local obstacle* techniques [13], [14] modify obstacle free trajectories using a perturbation function. Although this approach is computationally efficient, kinematic constraints have not been previously considered.

The *artificial potential field (APF)* [15] approach considers the environment as a potential field where the combinations of attraction and repulsion elements are used to represent the destination and obstacles, respectively. Continuous and smooth motion can be efficiently determined from closed-form expressions of the trajectory velocity. In general, APF methods may be stuck within local minima. However, *harmonic potential functions (HPFs)* are a special type of APFs that do not suffer from local minima [2], [3], [16]–[18]. The panel method [2], [17], [18] is an HPF approach that has been studied for motion planning within more complex obstacle environments. The obstacles are modeled as panel elements within an electrical potential field. However, kinematic constraints have not been studied in the panel method. Furthermore, the efficiency of the method decreases significantly as the number of obstacles increases.

Differential equations modeling the flow of fluids is one type of HPFs that has been used in motion planning for obstacle avoidance and inclusion of kinematic constraints [19]–[22]. The fluid flow approach in motion planning can efficiently produce natural looking trajectories. Closed-form velocity expressions of sink and doublet elements represent the target destination and obstacles, respectively. Additionally, nonholonomic motion in dynamically changing environments can be more easily achieved by situating a source element behind the robot [22]. Furthermore, the approach is suitable for multiple obstacle environments as the time complexity in computing the trajectory velocity increases linearly with the number of obstacles. However, this approach has only been studied for motion planning in 2-D environments with circular [19]–[21] and elliptical [22] obstacles as the governing differential equations are limited to modeling 2-D fluid flow.

In this paper, a fluid flow motion planning approach for 3-D nonholonomic mobile robots is proposed. Extending from 2-D fluid flow methods, closed-form expressions for the reference trajectory velocities are derived. The avoidance of spheroidal obstacles is achieved using the sphere theorem [23] and the Joukowski transform [24]. The use of HPFs and conformal

Manuscript received May 13, 2015; revised August 25, 2015; accepted September 22, 2015. Date of publication October 19, 2015; date of current version December 2, 2015. This paper was recommended for publication by Associate Editor L. Pallottino and Editor C. Torras upon evaluation of the reviewers' comments.

D. Lau is with Sorbonne Universités, UPMC University of Paris 6, UMR 7222, Institut des Systèmes Intelligents et de Robotique, F-75005 Paris, France, with CNRS, UMR 7222, Institut des Systèmes Intelligents et de Robotique, F-75005 Paris, France, and with the Melbourne School of Engineering, The University of Melbourne, Parkville, Vic. 3010, Australia (e-mail: laudt@unimelb.edu.au).

J. Eden and D. Oetomo are with the Melbourne School of Engineering, The University of Melbourne, Parkville, Vic. 3010, Australia (e-mail: j.eden2@student.unimelb.edu.au; doetomo@unimelb.edu.au).

Color versions of one or more of the figures in this paper are available online at <http://ieeexplore.ieee.org>.

Digital Object Identifier 10.1109/TRO.2015.2482078

mappings ensures that the proposed motion planning approach is free of local minima. Furthermore, through appropriate selection of the source and sink elements' strengths, it is shown that constraints in speed and curvature can be satisfied. The effectiveness of the proposed approach is illustrated through various example scenarios.

The proposed approach possesses the efficiency of 2-D fluid motion planners and the ability to consider kinematic constraints. Compared with existing HPF approaches, the proposed fluid motion planner is an efficient and intuitive approach that can be applied for a wide range of applications in 3-D environments, such as fixed-wing UAVs, quadrotors, or underwater vehicles. Obstacles with complex geometries can typically be encapsulated by spheroids [25], [26]. The presented work can be considered as a fundamental framework for 3-D fluid motion planning, where additional kinematic constraints and more complex scenarios can be incorporated. In [27], a similar fluid motion planning approach was used in the motion planning of three-link serial manipulators with nonconformal mappings. In comparison, this study uses conformal mappings and takes into consideration the satisfaction of kinematic constraints.

The remainder of the paper is organized as follows: Section II presents the environment model and avoidance of spheroidal obstacles. The satisfaction of kinematic constraints is described in Section III. The resulting simulated trajectories for a range of scenarios are presented and discussed in Section IV. Finally, Section V concludes the paper and presents areas of future work.

II. THREE-DIMENSIONAL MOTION PLANNING WITH SPHEROIDAL OBSTACLES

In this section, the extension of the 2-D fluid motion planning approach to 3-D environments is presented. From the avoidance of circular and elliptical obstacles in 2-D environments [19]–[22], the sphere theorem [23] and the 3-D Joukowski transform [24] are used to achieve obstacle avoidance of spheroidal obstacles.

The fundamental element of fluid motion planners is the *HPF* representing the fluid flow streamline equations. An HPF is a C^2 -continuous potential function $\phi(\mathbf{x})$ that has a Laplacian equal to zero $\nabla^2 \phi(\mathbf{x}) = 0$. As a result, one key feature of HPFs is that it does not possess any local minima. Defining the position of the robot center in Cartesian coordinates as $\mathbf{x} = [x \ y \ z]^T$, the gradient of the potential function $\phi(\mathbf{x})$ represents the velocity of the planned reference robot trajectory

$$\dot{\mathbf{x}} = \nabla \phi(\mathbf{x}). \quad (1)$$

For example, the potential function for a point charge located at $\mathbf{p} = [p_x \ p_y \ p_z]^T$ is defined as

$$\phi(\mathbf{x}) = -\frac{Q}{4\pi \|\mathbf{x} - \mathbf{p}\|} \quad (2)$$

where $Q \neq 0$ represents the strength of the charge. It can be shown that the potential function in (2) is an HPF since $\nabla^2 \phi(\mathbf{x}) = 0$. The point charge potential function can be used to model both source (repulsion) and sink (attraction) ele-

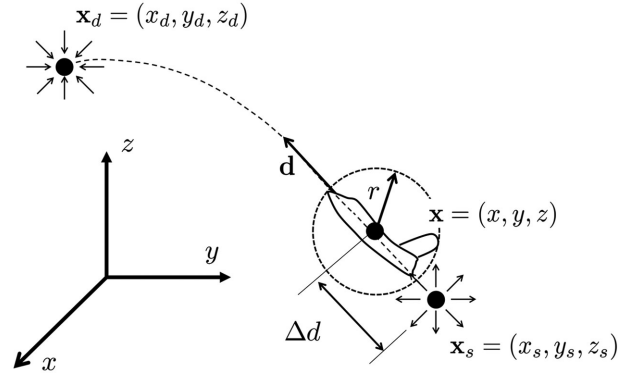


Fig. 1. Model of the environment showing the robot of radius r at location \mathbf{x} . A sink element is located at the destination location \mathbf{x}_d . To guide the robot on a nonholonomic trajectory, a source element is placed at a distance Δd behind the robot at location \mathbf{x}_s .

ments, where $Q > 0$ and $Q < 0$ represent source and sink point charges, respectively.

A. Environment Model

The model of the environment for the proposed 3-D motion planner is shown in Fig. 1. The robot's physical dimensions are considered by assuming that the robot can be encapsulated within a sphere of radius r . This radius can be considered when avoiding obstacles by incorporating it into the radius of the obstacles. The pose of the robot can be defined by the position of its center $\mathbf{x} = [x \ y \ z]^T$ expressed in Cartesian coordinates and its orientation $\mathbf{q} = [q_x \ q_y \ q_z \ \theta]^T$ represented in quaternion form. The heading direction of the robot \mathbf{d} can be defined by the unit vector

$$\mathbf{d} = \mathbf{q} \mathbf{q}_0 \mathbf{q}^{-1} \quad (3)$$

where $\mathbf{q}_0 = [1 \ 0 \ 0 \ 0]^T$ represents the inertial frame of the reference quaternion.

The target location $\mathbf{x}_d = [x_d \ y_d \ z_d]^T$ for the trajectory can be represented by a sink element of strength $Q_d > 0$, such that any streamlines in the environment will be attracted to this point. To guide the robot along a nonholonomic path, a source of strength $Q_s > 0$ is situated behind the robot in the direction of its heading. The influence of this source element will be mathematically described in Section III. From the heading direction vector (3), the position of the source element \mathbf{x}_s can be expressed as

$$\mathbf{x}_s = \mathbf{x} - \Delta d \cdot \mathbf{d} \quad (4)$$

where $\Delta d > 0$ represents a constant distance between the robot and the source location. It should be noted that both the distance of the source location Δd and the strength of the source Q_s have an effect on the speed of the robot's reference trajectory, where a decrease in Δd and an increase in Q_s both increase the speed of the reference trajectory. For mathematical convenience, the distance Δd is set as a constant and Q_s is selected to satisfy the required kinematic constraints.

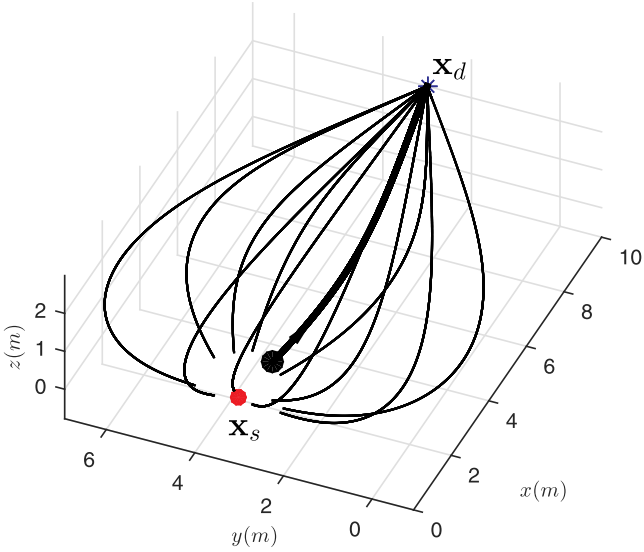


Fig. 2. Streamlines for the HPF in (5) when in an obstacle-free environment. The bold line shows the resulting trajectory if the robot is situated at the black circle.

From (2), the potential function for the system can be constructed from the superposition of the source and sink elements

$$\phi(\mathbf{x}) = \phi_s + \phi_d = -\frac{Q_s}{4\pi \|\mathbf{x} - \mathbf{x}_s\|} + \frac{Q_d}{4\pi \|\mathbf{x} - \mathbf{x}_d\|}. \quad (5)$$

Taking the gradient of (5) produces the instantaneous velocities of the planned trajectory of the robot center $\dot{\mathbf{x}} = \nabla\phi$. The planned trajectory of the robot center can then be determined by numerically integrating $\dot{\mathbf{x}}$ at each sample time step for the discrete-time system. Since ϕ_s and ϕ_d are HPFs, ϕ from (5) is also an HPF ($\nabla^2\phi(\mathbf{x}) = \nabla^2\phi_s(\mathbf{x}) + \nabla^2\phi_d(\mathbf{x}) = 0$) and does not possess any local minimum. As a result, the resulting trajectory $\mathbf{x}(t)$ would not get stuck within any local minimum. Fig. 2 shows the resulting streamlines for the HPF in (5), where the bolded line is the example trajectory when the particle (robot center) is situated at the black dot.

It should be noted that at $\mathbf{x} = \mathbf{x}_d$, the potential function (5) is mathematically undefined and results in a singularity. This is a natural property of fluid flow potential functions. In the proposed motion planner, the destination point will be the robot's next reference location if the robot is able to reach the destination in the next instance in time given the maximum speed V_{\max} of the robot. Furthermore, the motion planning algorithm will be temporarily deactivated, and the robot will remain at the location until the destination point changes and the motion planner is activated again.

B. Spheroidal Obstacle Trajectory Planning

Applying the sphere theorem [23] on (5) allows the potential function $\phi_S(\mathbf{x})$ for the environment with a spherical obstacle of radius R to be expressed as

$$\phi_S = \phi(\mathbf{x}) + \frac{R}{\|\mathbf{x}\|} \phi\left(\frac{R^2\mathbf{x}}{\|\mathbf{x}\|^2}\right) - \frac{2}{R\|\mathbf{x}\|} \int_0^R s\phi\left(\frac{s^2\mathbf{x}}{\|\mathbf{x}\|^2}\right) ds. \quad (6)$$

It should be noted that the sphere theorem (6) assumes that the spherical object is located at the origin. For a spherical obstacle with its center located at \mathbf{x}_o , a translational change of variables $\tilde{\mathbf{x}} = \mathbf{x} - \mathbf{x}_o$ could be used to determine $\dot{\tilde{\mathbf{x}}} = \nabla\phi_S(\tilde{\mathbf{x}})$. Fig. 3(a) shows the streamlines for the potential function after applying the sphere theorem (6) on the obstacle-free streamlines shown in Fig. 2. Since the sphere theorem (6), also known as the Kelvin transform, preserves the HPF property [28], the resulting potential function $\phi_S(\mathbf{x})$ is an HPF given that $\phi(\mathbf{x})$ from (5) is also an HPF.

The 3-D Joukowski transform is a conformal mapping that can be used to transform the position ${}^c\tilde{\mathbf{x}} = [{}^c\tilde{x} \quad {}^c\tilde{y} \quad {}^c\tilde{z}]^T$ on the streamlines about a spherical object (6) of radius R to the corresponding position ${}^e\tilde{\mathbf{x}} = [{}^e\tilde{x} \quad {}^e\tilde{y} \quad {}^e\tilde{z}]^T$ on the flow over a spheroid. This conformal mapping can be expressed as

$${}^e\tilde{x} = \frac{{}^c\tilde{x}}{2} + \frac{\lambda^3 {}^c\tilde{x}}{\|{}^c\tilde{\mathbf{x}}\|^3}, \quad {}^e\tilde{y} = \frac{{}^c\tilde{y}}{2} + \frac{\lambda^3 {}^c\tilde{y}}{\|{}^c\tilde{\mathbf{x}}\|^3}, \quad {}^e\tilde{z} = {}^c\tilde{z} - \frac{\lambda^3 {}^c\tilde{z}}{\|{}^c\tilde{\mathbf{x}}\|^3} \quad (7)$$

where $-\frac{R}{\sqrt{2}} \leq \lambda \leq R$ represents the transformation constant. The radius of the circle a for the circular cross-section and radius of the elliptical axis b can be expressed as

$$a = \frac{R}{2} + \frac{\lambda^3}{R^2}, \quad b = R - \frac{\lambda^3}{R^2}. \quad (8)$$

For mathematical convenience, the Joukowski transform between ${}^c\tilde{\mathbf{x}}$ and ${}^e\tilde{\mathbf{x}}$ (7) assumes that the spheroidal object is centered at the origin with the major circular cross section in the xy plane. The trajectory to avoid a single spheroidal obstacle can then be determined by applying the 3-D Joukowski transform (7) on the equivalent trajectory about a spherical obstacle of radius R . Fig. 3(b) shows the resulting streamlines when the Joukowski theorem transform (7) has been applied on the sphere avoidance streamlines in Fig. 3(a).

However, it should be noted that (7) is a transformation at positional level coordinates. As shown later in Section III, the selection of appropriate source and sink strengths to satisfy the kinematic constraints at velocity level requires expression of the trajectory velocity. The velocity of the trajectory to avoid a spheroidal obstacle ${}^e\dot{\tilde{\mathbf{x}}}$ can be determined by taking the derivative of the Joukowski transform from (7), where

$$\begin{aligned} {}^e\dot{\tilde{x}} &= \frac{{}^c\dot{\tilde{x}}}{2} + \frac{\lambda^3 (\|{}^c\tilde{\mathbf{x}}\|^3 {}^c\dot{\tilde{x}} - 3\|{}^c\tilde{\mathbf{x}}\| {}^c\tilde{\mathbf{x}} ({}^c\tilde{\mathbf{x}} \cdot {}^c\dot{\tilde{\mathbf{x}}}))}{\|{}^c\tilde{\mathbf{x}}\|^6} \\ {}^e\dot{\tilde{y}} &= \frac{{}^c\dot{\tilde{y}}}{2} + \frac{\lambda^3 (\|{}^c\tilde{\mathbf{x}}\|^3 {}^c\dot{\tilde{y}} - 3\|{}^c\tilde{\mathbf{x}}\| {}^c\tilde{\mathbf{x}} ({}^c\tilde{\mathbf{x}} \cdot {}^c\dot{\tilde{\mathbf{x}}}))}{\|{}^c\tilde{\mathbf{x}}\|^6} \\ {}^e\dot{\tilde{z}} &= {}^c\dot{\tilde{z}} - \frac{\lambda^3 (\|{}^c\tilde{\mathbf{x}}\|^3 {}^c\dot{\tilde{z}} - 3\|{}^c\tilde{\mathbf{x}}\| {}^c\tilde{\mathbf{x}} ({}^c\tilde{\mathbf{x}} \cdot {}^c\dot{\tilde{\mathbf{x}}}))}{\|{}^c\tilde{\mathbf{x}}\|^6}. \end{aligned} \quad (9)$$

The velocity level transform (9) allows the velocity of the trajectory to avoid a spherical obstacle ${}^c\dot{\tilde{\mathbf{x}}} = \nabla\phi_S({}^c\tilde{\mathbf{x}})$ to be transformed to the trajectory velocity in the presence of a spheroidal obstacle.

For a spheroidal obstacle located at \mathbf{x}_o with a rotation of $R_s \in SO(3)$ to rotate the spheroidal obstacle to align its major

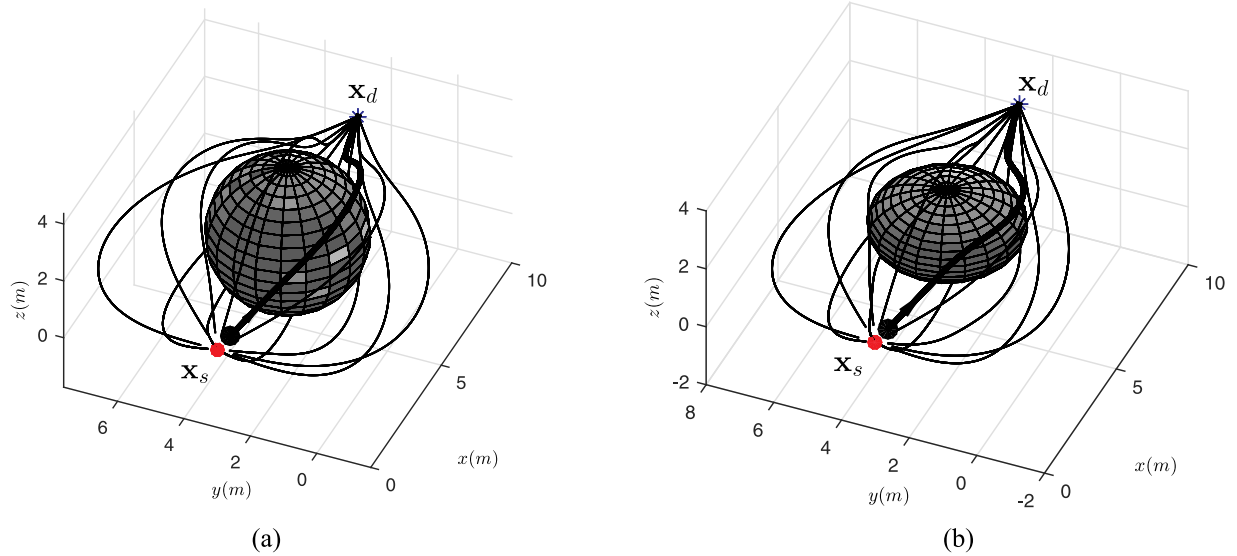


Fig. 3. Streamlines for the flow from Fig. 2 around (a) a spherical object and (b) a spheroidal object after the Joukowski transform. The bold line shows the chosen trajectory when the robot is situated at the black circle. (a) Streamlines about a sphere. (b) Streamlines about a spheroid.

circular cross section to the xy plane, a change of variable

$${}^e\tilde{\mathbf{x}} = R_s(\mathbf{x} - \mathbf{x}_o) \quad (10)$$

can be introduced. The transformed variables for the robot position ${}^e\tilde{\mathbf{x}}$, source ${}^e\tilde{\mathbf{x}}_s$ and sink ${}^e\tilde{\mathbf{x}}_d$ locations, will then be used within the Joukowski transform (9), sphere theorem (6), and the source–sink potential function (5). The resulting velocity vector ${}^e\dot{\tilde{\mathbf{x}}}$ must be rotated back into the original coordinates through $\dot{\mathbf{x}} = R_s^{-1} {}^e\dot{\tilde{\mathbf{x}}}$.

Since the presented potential functions assume a point mass particle with zero radius, the radius of the robot r must be added onto the dimensions of the spheroidal obstacle a_{obs} and b_{obs} when used within motion planning, where $a = a_{\text{obs}} + r$, $b = b_{\text{obs}} + r$ (8). The overall procedure to determine the instantaneous velocity of the robot to avoid a single spheroidal obstacle is summarized in Algorithm 1. Fig. 4 shows example trajectories using the proposed motion planning algorithm.

The trajectories from Fig. 4(a) and (b) show that the robot with radius r is able to navigate to the target destination along a smooth trajectory while avoiding spheroidal obstacles of different sizes.

C. Multiple Obstacle Avoidance

Section II-B presented the fluid flow 3-D motion planning approach to avoid a single obstacle. Multiple obstacle avoidance fluid flow motion planning in 2-D has been proposed in [19]. Since the presented potential functions to avoid a single spheroidal obstacle in 3-D are HPFs, the weighted superposition [19] of single obstacle avoidance trajectories could also be used in this study. Hence, the velocity of the planned trajectory in an n obstacle environment can be expressed as

$$\dot{\mathbf{x}} = \sum_{i=1}^n \alpha_i(\mathbf{x}) \dot{\tilde{\mathbf{x}}}_i \quad (11)$$

Algorithm 1 Motion planning with a single spheroidal obstacle

Require: Robot position \mathbf{x} , heading vector \mathbf{d} and radius r
Require: Robot target location \mathbf{x}_d
Require: Spheroid obstacle position \mathbf{x}_{obs} , rotation R_s
Require: Spheroid obstacle dimensions $a_{\text{obs}}, b_{\text{obs}}$
Ensure: Velocity of planned reference robot trajectory $\dot{\mathbf{x}}$
 $a \leftarrow a_{\text{obs}} + r$ to incorporate robot radius
 $b \leftarrow b_{\text{obs}} + r$ to incorporate robot radius
 $\lambda, R \leftarrow$ Solve from a, b using (8)
 $\mathbf{x}_s \leftarrow \mathbf{x} - \Delta d \cdot \mathbf{d}$ to determine the sink location using (4)
 ${}^e\tilde{\mathbf{x}}, {}^e\tilde{\mathbf{x}}_s, {}^e\tilde{\mathbf{x}}_d \leftarrow R_s(\mathbf{x} - \mathbf{x}_o), R_s(\mathbf{x}_s - \mathbf{x}_o), R_s(\mathbf{x}_d - \mathbf{x}_o)$ using (10)
 ${}^c\tilde{\mathbf{x}}, {}^c\tilde{\mathbf{x}}_s, {}^c\tilde{\mathbf{x}}_d \leftarrow$ Transform from ${}^e\tilde{\mathbf{x}}, {}^e\tilde{\mathbf{x}}_s, {}^e\tilde{\mathbf{x}}_d$ using (7)¹
 ${}^c\dot{\tilde{\mathbf{x}}} \leftarrow \nabla\phi_S({}^c\tilde{\mathbf{x}})$ with ϕ as (5) with ${}^c\tilde{\mathbf{x}}, {}^c\tilde{\mathbf{x}}_d, {}^c\tilde{\mathbf{x}}_s$ using (6)
 ${}^e\dot{\tilde{\mathbf{x}}} \leftarrow$ Determine with ${}^c\dot{\tilde{\mathbf{x}}}$ and ${}^c\tilde{\mathbf{x}}$ using (9)
 $\dot{\mathbf{x}} \leftarrow R_s^{-1} {}^e\dot{\tilde{\mathbf{x}}}$ transform velocity back to original frame

where $\alpha_i \geq 0$ and $\dot{\tilde{\mathbf{x}}}_i = \nabla\phi_i$ represent the weighting and velocity of the planned trajectory, respectively, for the i th spheroidal obstacle. It should be noted that the source strength Q_s and sink strength Q_d are the same for all of the individual obstacles. It will be shown in Section III that this is convenient for the selection of source and sink strengths to satisfy constraints on the planned trajectory.

In the proposed path planner, the weighting function $\alpha_i(\mathbf{x})$ is chosen to be

$$\alpha_i(\mathbf{x}) = \prod_{j \neq i}^n \frac{d_j^4}{d_i^4 + d_j^4} \quad (12)$$

where d_i represents the shortest distance between the robot and surface of the obstacle i . The proposed weighting function

¹The inverse of (7) can be determined numerically using Newton root finding methods.

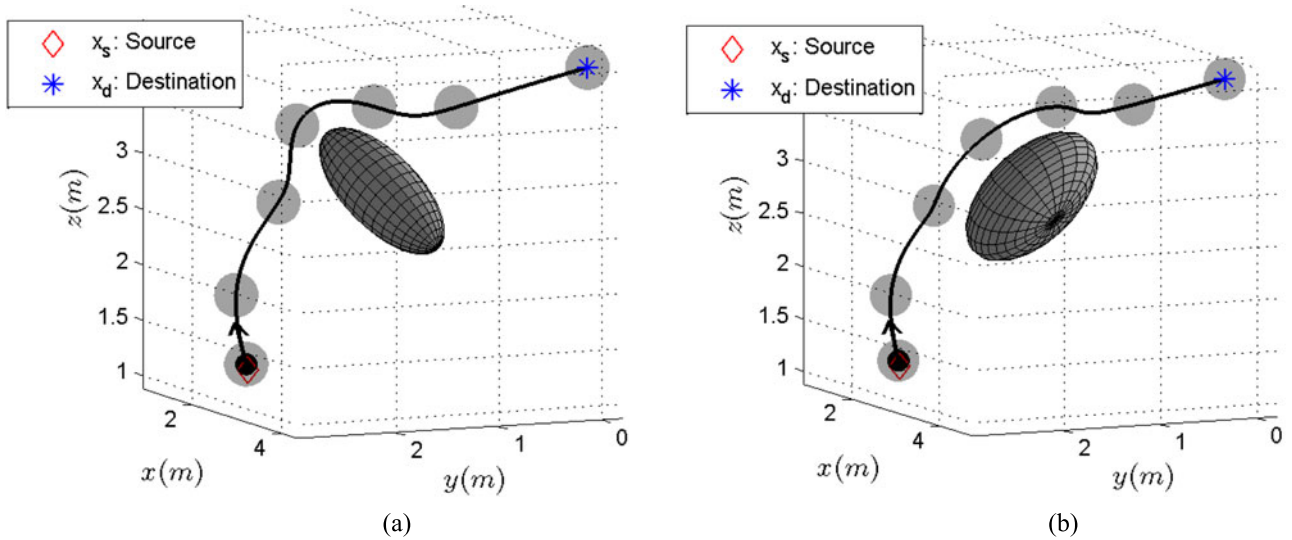


Fig. 4. Examples of single spheroid avoidance, where (a) shows avoidance of an obstacle with dimensions $a = 0.5$ m, $b = 1$ m and (b) shows avoidance of an obstacle with dimensions $a = 1$ m, $b = 0.5$ m. The gray spheres show the robot at different instances in time along the trajectory. (a) $a = 0.5$, $b = 1$. (b) $a = 1$, $b = 0.5$.

(12) satisfies the required properties from [19], where the primary difference is that (12) would favor the following of the streamline to avoid the closest obstacle by increasing the power of the distance terms d_i^4 and d_j^4 .

D. Convergence of the Motion Planner

In Sections II-A and II-B, it was shown that the potential function ϕ_S used to generate the trajectory for the avoidance of a single spherical obstacle is an HPF and hence is free of any local minima. Furthermore, since the potential function in (5) possesses only a single sink (attractive element), all streamlines must converge to a unique global minimum of the potential function, the destination goal location x_d . What remains is to show that the planned trajectory to avoid multiple spheroidal obstacles presented in Section II-C also converges to the goal x_d and is free of getting stuck within local minima.

First, the Joukowski transform in 3-D, represented by (7) and (9), is a one-to-one quasi-conformal mapping that preserves the direction of the flow field. As such, since the potential function for spherical obstacle avoidance is an HPF with a unique global minimum, the resulting trajectory to avoid a single spheroidal obstacle using the Joukowski transform must also have a unique global minimum (the target destination x_d).

Second, every trajectory x_i to avoid a single spheroidal obstacle possesses the following properties.

- 1) All trajectories have the same target destination x_d (location of the sink).
- 2) The velocity $\dot{x}_i = \nabla\phi_i$ for every trajectory at every instance in time must be nonzero $\dot{x}_i \neq \mathbf{0}$ and always contain a positive component towards the goal x_d since $\phi_i \forall i$ is an HPF.

Assuming that all of the obstacles are not overlapping or touching, the weighting scheme [19] described in Section II-C ensures that at least one of the weighting terms is positive $\exists i : \alpha_i > 0$. As a result, the resulting trajectory (11) will never

be zero and also contain a positive component toward the goal x_d . In summary, compared with traditional APF approaches, the use of HPFs within the proposed motion planning scheme is advantageous to ensure that the robot does not get stuck within any local minima in the presence of multiple obstacles.

III. KINEMATIC CONSTRAINTS

Previous fluid flow motion planner studies have not considered the satisfaction of kinematic constraints, such as path curvature. In addition to the nonholonomic constraint, the physical robot geometry and operating environment may result in kinematic constraints. In Section II, the source and sink strengths, Q_s and Q_d , respectively, are assumed to be constant values. In this section, it will be shown that kinematic constraints can be satisfied by appropriate selection of these strengths.

As observed from Section II, the velocity \dot{x}_i of the planned trajectory for obstacle i can be expressed as a sum of source v_{i_s} and a sink v_{i_d} velocity components that are computed from the transforms on the potential functions ϕ_s and ϕ_d in (5), respectively. The velocity \dot{x}_i can, therefore, be expressed as $\dot{x}_i = v_{i_s} + v_{i_d}$, where it should be noted that terms v_{i_s} and v_{i_d} are the velocities in the presence of spheroidal obstacles.

Since the source strength Q_s and sink strength Q_d are selected to be same for all x_i to avoid the obstacles, the expression of \dot{x}_i can always be expressed as $\dot{x}_i = Q_s \hat{v}_{i_s} + Q_d \hat{v}_{i_d}$, where \hat{v}_{i_s} and \hat{v}_{i_d} are the velocities v_{i_s} and v_{i_d} , respectively, with the element strengths extracted. Hence, the velocity of the planned trajectory under multiple obstacles from (11) can be expressed as

$$\mathbf{v} = \sum_i \alpha_i \dot{x}_i = Q_s \hat{\mathbf{v}}_s + Q_d \hat{\mathbf{v}}_d \quad (13)$$

where $\hat{\mathbf{v}}_s = \sum_i \alpha_i \hat{v}_{i_s}$ and $\hat{\mathbf{v}}_d = \sum_i \alpha_i \hat{v}_{i_d}$.

By varying the source and sink strengths, it can be observed that different values of Q_s and Q_d with the same source to

sink ratio $Q_r = \frac{Q_d}{Q_s}$ do not have an effect on the resulting path when the distance Δd of the source element behind the robot is constant. Increasing Q_s and Q_d under the same ratio results in an increase in only the trajectory speed. Hence, for the convenience of applying the constraints in speed and path curvature, the planned trajectory velocity from (13) can be expressed in the form

$$\mathbf{v} = Q_a(\hat{\mathbf{v}}_s - Q_r \hat{\mathbf{v}}_d) \quad (14)$$

where $Q_a = Q_s$ and $Q_r = \frac{Q_d}{Q_s}$ denote the amplitude and ratio constants of the source–sink strengths, respectively. The implication of such a representation is that the variation of Q_a for a fixed Q_r has a linear effect on the trajectory speed, and Q_r can also be selected for a particular Q_a to achieve curvature constraints in the path. Sections III-A and III-B show how different constraints can be satisfied through appropriate selection of Q_a and Q_r .

It will be shown in the following that the addition of a source element behind the robot, as described in Section II-A, is greatly beneficial in guiding the planned robot trajectory along a non-holonomic path. The nonholonomic constraint for a 3-D mobile robot restricts its velocity $\dot{\mathbf{x}} = [\dot{x} \ \dot{y} \ \dot{z}]^T$ to follow its heading direction and the constraints can be represented as

$$\begin{aligned} \dot{x} \sin \theta - \dot{y} \cos \theta &= 0 \\ \sqrt{\dot{x}^2 + \dot{y}^2 + \dot{z}^2} \cos \psi - \dot{z} &= 0 \end{aligned} \quad (15)$$

where θ and ψ represent the spherical polar and azimuth angles, respectively. The polar and azimuth angles can be determined from the heading direction of the robot \mathbf{d} , where

$$\mathbf{d} = [\cos \theta \sin \psi \ \sin \theta \sin \psi \ \cos \psi]^T. \quad (16)$$

In the scenario that the effect of the source is much greater than that of the sink, where $\|\nabla \phi_s\| \gg \|\nabla \phi_d\|$ from (5), then the potential function is approximately equivalent to that of the source element $\phi \approx \phi_s$. Using the definitions of (16) and (4), the trajectory velocities can be determined by taking the gradient of ϕ_s from (5) as

$$\dot{x} = \frac{Q_s \cos \theta \sin \psi}{4\pi D^2}, \quad \dot{y} = \frac{Q_s \sin \theta \sin \psi}{4\pi D^2}, \quad \dot{z} = \frac{Q_s \cos \psi}{4\pi D^2} \quad (17)$$

where $D = \Delta d$. It can be observed that the velocities from (17) satisfy the nonholonomic constraints (15). However, due to the presence of the sink element, the resulting planned trajectory only satisfies the nonholonomic constraints approximately to guide the robot on a nonholonomic path. In practice, the non-holonomic robot will use the trajectory from the motion planner as a reference input at each discrete-time instance.

A. Constraint in Speed

The velocity expression from (14) allows the instantaneous robot speed $\|\mathbf{v}\|$ to be expressed in the form

$$\|\mathbf{v}\| = Q_a \sqrt{a_2 Q_r^2 + a_1 Q_r + a_0} \quad (18)$$

where the coefficients are $a_2 = \|\hat{\mathbf{v}}_d\|^2$, $a_1 = -2\hat{\mathbf{v}}_s \cdot \hat{\mathbf{v}}_d$ and $a_0 = \|\hat{\mathbf{v}}_s\|^2$. The coefficients a_2 , a_1 , and a_0 can be computed

with the knowledge of the environment, such as the source and sink locations. Considering a maximum allowable speed V_{\max} , the speed constraint $\|\mathbf{v}\| \leq V_{\max}$ applied to (18) results in the following relationship:

$$Q_a \sqrt{a_2 Q_r^2 + a_1 Q_r + a_0} \leq V_{\max}. \quad (19)$$

Observing that the natural behavior for a constant Q_a and Q_r is that the speed of the trajectory would increase significantly as the robot approaches the destination \mathbf{x}_d , the constraint (19) will naturally decrease the amplitude constant Q_a as the robot approaches \mathbf{x}_d .

B. Constraint in Curvature

The local curvature of the trajectory at any instance in time can be expressed with respect to the instantaneous velocity and acceleration

$$\kappa(t) = \frac{\sqrt{(\dot{y}\ddot{z} - \dot{z}\ddot{y})^2 + (\dot{x}\ddot{z} - \dot{z}\ddot{x})^2 + (\dot{x}\ddot{y} - \dot{y}\ddot{x})^2}}{\|\mathbf{v}\|^3}. \quad (20)$$

Note that curvature is defined to be $\kappa = \frac{1}{\rho}$, where ρ is the radius of curvature. On physical discrete-time systems, the acceleration at time sample k can be expressed using finite difference as

$$\dot{\mathbf{v}}_k = \frac{\mathbf{v}_k - \mathbf{v}_{k-1}}{\Delta t} \quad (21)$$

where Δt is the sample time, and $\mathbf{v}_k = [\dot{x}_k \ \dot{y}_k \ \dot{z}_k]^T$ and \mathbf{v}_{k-1} represent the velocities at time samples t_k and t_{k-1} , respectively. Since at time $t = t_k$, the velocity \mathbf{v}_{k-1} is known, and from (14), $\mathbf{v}_k = Q_a(\hat{\mathbf{v}}_s + Q_r \hat{\mathbf{v}}_d)$, the aim is to determine appropriate values of $Q_a > 0$ and $Q_r > 0$ to satisfy the curvature constraint $\kappa \leq \kappa_{\max}$. Substitution of (18) and (21) into (20) allows the discretized curvature κ_k at time $t = t_k$ to be expressed with respect to Q_r as

$$\kappa_k = \frac{\sqrt{b_2 Q_r^2 + b_1 Q_r + b_0}}{\Delta t \|\mathbf{v}\|^2 \sqrt{a_2 Q_r^2 + a_1 Q_r + a_0}} \quad (22)$$

where b_2 , b_1 , b_0 , a_2 , a_1 , and a_0 are functions of \mathbf{v}_{k-1} , $\hat{\mathbf{v}}_s$, and $\hat{\mathbf{v}}_d$.

Considering a maximum curvature constraint $\kappa \leq \kappa_{\max}$ on the system, the curvature expression from (22) results in the following constraint:

$$C_2 Q_r^2 + C_1 Q_r + C_0 \leq 0 \quad (23)$$

where $C_i = (b_i - \kappa_{\max}^2 \Delta t^2 a_i \|\mathbf{v}\|^4)$ for $i = 0, 1, 2$. From (23), the ratio constant Q_r can be expressed as function of the desired speed $\|\mathbf{v}\|$.

As a result, the problem of generating a reference trajectory that satisfies both speed and curvature constraints can be solved by selecting appropriate amplitude and ratio constants using (19) and (23). To remain on the same streamline in the fluid flow field for as much as possible while generating the trajectory, it is desired that the ratio constant Q_r is maintained as a constant value. To achieve this in the proposed motion planner, a new Q_r is selected only if the previous Q_r violates the curvature constraint (23). It will be demonstrated in the first example of Section IV-A that the value of Q_r does not change by an arbitrary

amount if κ_{\max} in (23) does not change by an arbitrary amount. Sudden changes in Q_r are undesired as this would result in sudden changes in the resulting reference velocity.

C. Feasibility of the Trajectory

In the presence of constraints, it is important to consider the existence of a feasible solution trajectory. In this section, two aspects related to the feasibility and existence of solution of the proposed motion planner are presented.

1) *Arrangement of Obstacles*: In the presented scheme to avoid multiple obstacles (11) with the weighting function (12), the avoidance of every obstacle is achieved by having higher weights to avoid the obstacle closest to the robot. As a result, when the robot is infinitesimally close to the boundary of the obstacle, the streamline will flow on the surface of the obstacle and avoid it. As such, the proposed motion planner requires that no obstacles overlap with each other. It can be regarded the responsibility of a higher level algorithm to group overlapping obstacles into one single obstacle for the motion planner. Given a robot of radius r , the spheroidal objects of dimensions $a = a_{\text{obs}} + r$ and $b = b_{\text{obs}} + r$ should not overlap. Practically, this means that the proposed motion planner requires that there is enough space between obstacles such that the robot can pass through.

2) *Feasible Source and Sink Strengths*: As presented in Sections III-A and III-B, constraints in speed and curvature could be satisfied through appropriate selections of the source and sink strengths represented by Q_a and Q_r . However, given the nature of the constraints, as observed mathematically in (19) and (23), there are scenarios in which no feasible solutions exist to satisfy the speed constraint $\|\mathbf{v}\| \leq V_{\max}$ and curvature constraint $\kappa \leq \kappa_{\max}$. Mathematically, solutions to the quadratic inequality (23), where $Q_r > 0$, exist if either:

- 1) $C_2 \leq 0$; or
- 2) the following three conditions are all satisfied: $C_2 > 0$, $C_1^2 - 4C_2C_0 \geq 0$ and $-C_1 + \sqrt{C_1^2 - 4C_2C_0} > 0$.

Since the terms $C_i = (b_i - \kappa_{\max}^2 \Delta t^2 a_i \|\mathbf{v}\|^4)$ for $i = 1, 2, 3$ are functions of κ_{\max} and $\|\mathbf{v}\|$, solutions to valid source and sink strengths that satisfy all of the constraints exist if either of the conditions above could be achieved for any $\|\mathbf{v}\| \leq V_{\max}$. However, if none of the conditions could not be satisfied for speed $\|\mathbf{v}\| \leq V_{\max}$, then the constraints $\|\mathbf{v}\| \leq V_{\max}$ and $\kappa \leq \kappa_{\max}$ are in conflict and the motion planner would be unable to produce a trajectory to satisfy all of the constraints. Physically, this corresponds to the scenario where κ_{\max} is so small such that the robot is not allowed to turn to avoid obstacles or to reach the destination location. For example, the constraint $\kappa_{\max} = 0$ corresponds to a constraint that the robot can only travel straight in its heading direction, and if the destination is not on this line, the constraint would result in no valid solutions for the motion planner.

IV. RESULTS AND DISCUSSION

The ability for the proposed motion planner to navigate within 3-D environments while avoiding multiple spheroidal obstacles and satisfying kinematic constraints is shown in this section.

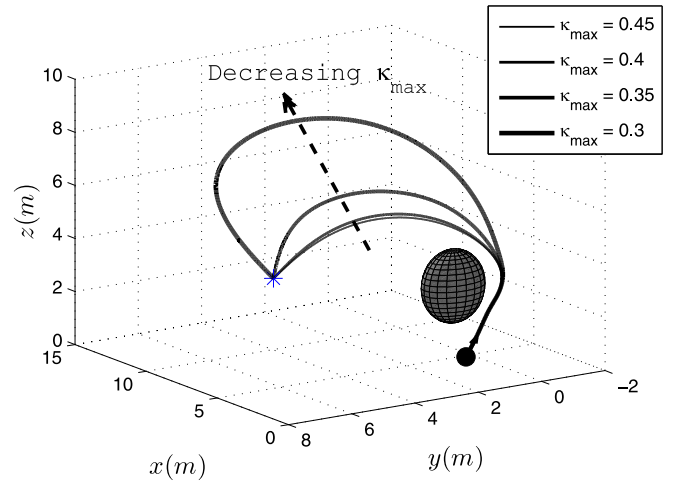


Fig. 5. Trajectories under various maximum curvature constraints. As the maximum curvature decreased from $\kappa_{\max} = 0.3$ to $\kappa_{\max} = 0.45$, the resulting trajectory performed a wider turn to reach the destination.

Three different example scenarios have been selected to demonstrate this.

- 1) *Example 1*: Single obstacle with a varying maximum curvature constraint.
- 2) *Example 2*: Avoidance of multiple spheroidal obstacles.
- 3) *Example 3*: Avoidance of multiple spheroidal obstacles subject to a maximum curvature constraint.

A. Simulation Examples

1) *Varying Maximum Curvature Constraint*: In the first example, the ability for the proposed 3-D fluid flow motion planner to satisfy maximum curvature constraints as formulated in Section III-B is demonstrated. Fig. 5 shows the planned trajectories to reach the destination while avoiding the obstacle under various maximum curvature κ_{\max} constraints. The speed of the trajectory was set as $\|\mathbf{v}\| = 1$ m/s for all cases. The source–sink ratio Q_r and amplitude constant Q_a were determined using (23) and (19), respectively. The ratio constant was initially set to $Q_r = 1$ for all four trajectories.

It can be observed that for different κ_{\max} constraints, the motion planner is able to produce smooth trajectories while reaching the target destination. Fig. 6 shows the curvature profiles $\kappa(t)$ for the trajectories under the constraints $\kappa_{\max} = 0.45$ m⁻¹ and $\kappa_{\max} = 0.30$ m⁻¹. It can be observed that the constraints in curvature were satisfied for the entire planned trajectory. As a result of lowering the κ_{\max} constraint, the robot must make a turn of larger radius and hence requiring a longer time to reach the destination since $\|\mathbf{v}\| = 1$ m/s for all four trajectories. The trajectory with $\kappa_{\max} = 0.30$ m⁻¹ in Fig. 6(b) took a total duration of 24.5 s to reach the destination compared with 13.5 s for $\kappa_{\max} = 0.45$ m⁻¹ in Fig. 6(a).

Fig. 7 shows how the adjustment of Q_r is performed in order to satisfy the maximum curvature constraint. It can be observed in Figs. 6(a) and 7(a) that for $Q_r = 1$, the curvature for the trajectory does not exceed the constraint $\kappa_{\max} = 0.45$ m⁻¹. As a result, the ratio constant of $Q_r = 1$ was used for the generation of the entire trajectory. However, this curvature profile would

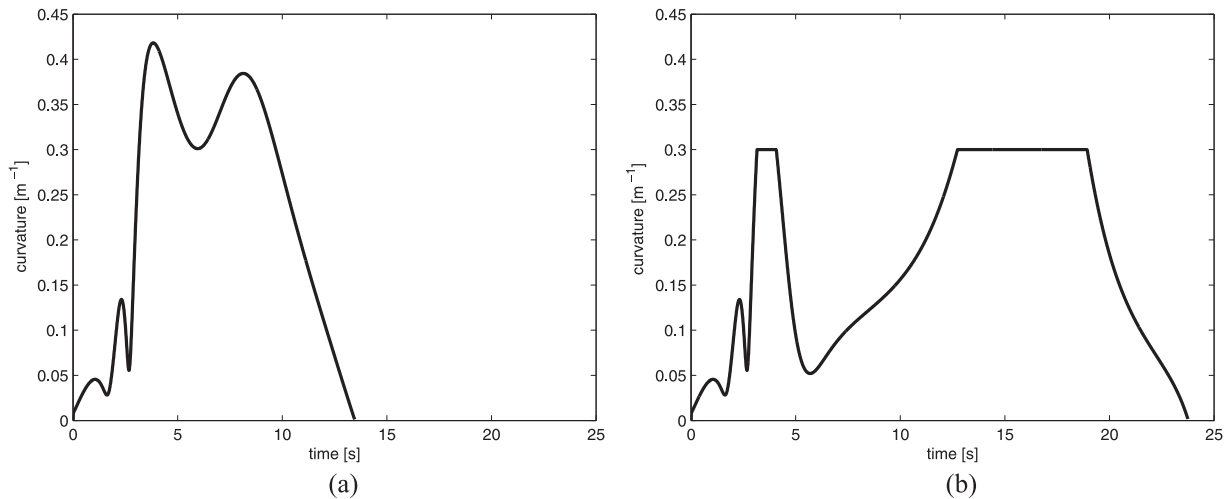


Fig. 6. Curvature profiles $\kappa(t)$ for (a) $\kappa_{\max} = 0.45 \text{ m}^{-1}$ and (b) $\kappa_{\max} = 0.3 \text{ m}^{-1}$.

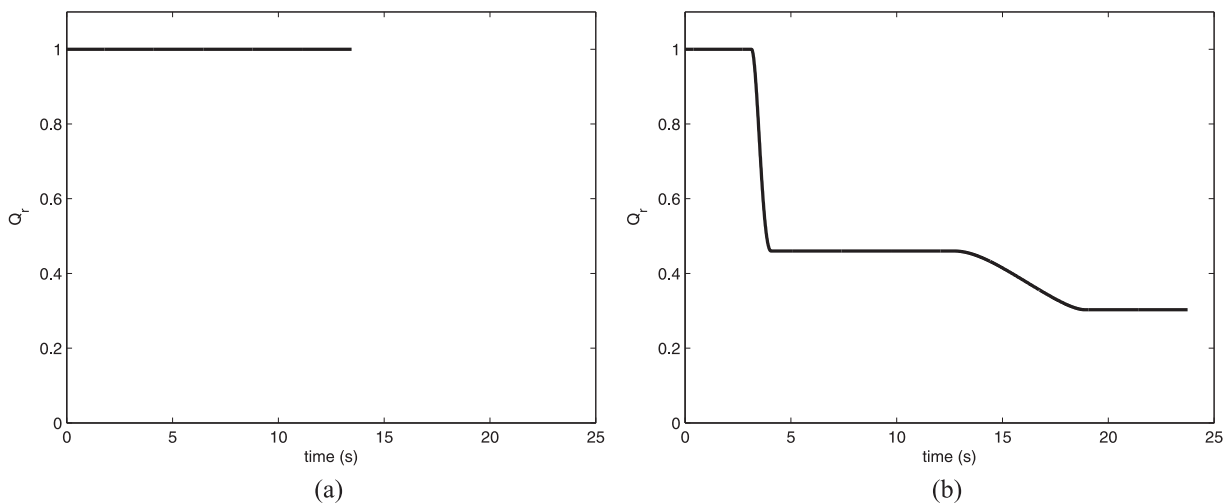


Fig. 7. Source-sink ratio profiles $Q_r(t)$ for (a) $\kappa_{\max} = 0.45 \text{ m}^{-1}$ and (b) $\kappa_{\max} = 0.3 \text{ m}^{-1}$.

violate the constraint $\kappa_{\max} = 0.30 \text{ m}^{-1}$. As observed in Fig. 7(b), at the first instance in time, $t = 3 \text{ s}$, when the constraint would violate, the motion planner adjusted the value of Q_r such that the constraint was satisfied. Between $t = 4 \text{ s}$ and $t = 12.5 \text{ s}$, the curvature remained within the constraint without requiring a change in Q_r . However, the constraint was active again between $t = 12.5 \text{ s}$ and $t = 19 \text{ s}$, and hence, the value of Q_r was continuously adjusted to ensure that the constraint was met. This example serves to show that the adjustment of the source and sink ratios allows kinematic constraints at velocity level to be satisfied.

2) *Multiple Obstacle Avoidance*: This example demonstrates the ability for the proposed motion planner to avoid multiple obstacles. The environment containing three spheroidal obstacles of varying obstacle sizes is shown in Fig. 8. Starting at a position of $\mathbf{x}_{\text{init}} = [1 \ 3 \ 2]^T$, the destination location was set to be $\mathbf{x}_d = [10 \ 3 \ 2]^T$. Fig. 8(a) and (b) shows the xz view (front view) and xy view (top view) of the resulting planned

trajectory. From the top view, it can be observed that the motion planner is able to plan a trajectory that can avoid all three obstacles.

To illustrate how the motion planner handles the avoidance of multiple obstacles using (11), the weights α_i from (12) are shown in Fig. 9.

From the weights $\alpha_i(t)$ for obstacles $i = 1, 2$, and 3 , it can be observed how the avoidance of multiple obstacles is achieved through combining the streamlines to avoid the individual obstacles. For example, from $t = 0 \text{ s}$ to $t \approx 3 \text{ s}$, since the robot is much closer to obstacle 1 compared with obstacles 2 and 3, the weight of $\alpha_1 \approx 1$ and $\alpha_2 \approx \alpha_3 \approx 0$ was observed. As a result, the trajectory $\dot{\mathbf{x}}_1$ to avoid obstacle 1 is the dominating trajectory that largely contributes to the resulting planned trajectory $\dot{\mathbf{x}} \approx \dot{\mathbf{x}}_1$. This is the same for obstacles 2 and 3 for the time periods $4.5 \leq t \leq 6 \text{ s}$ and $6.5 \leq t \leq 10 \text{ s}$, respectively. For these periods, the motion planner is effectively performing single obstacle avoidance.

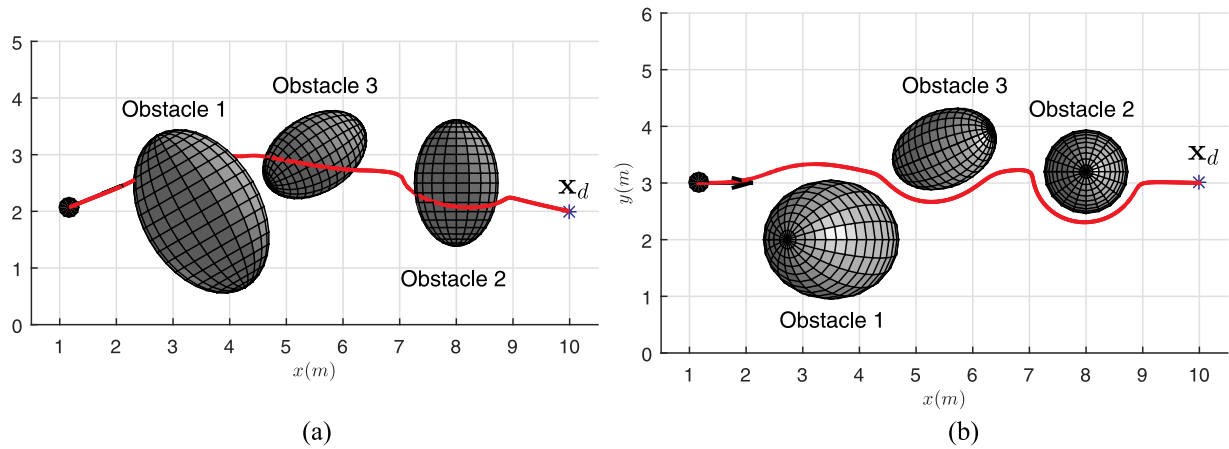


Fig. 8. Resulting trajectory to avoid multiple spheroidal obstacles simultaneously. (a) xz view. (b) xy view.

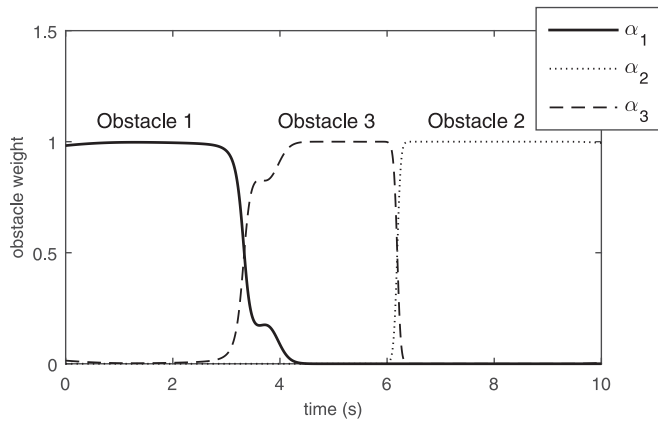
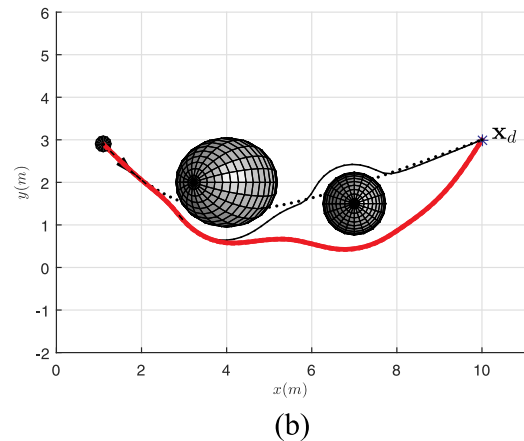
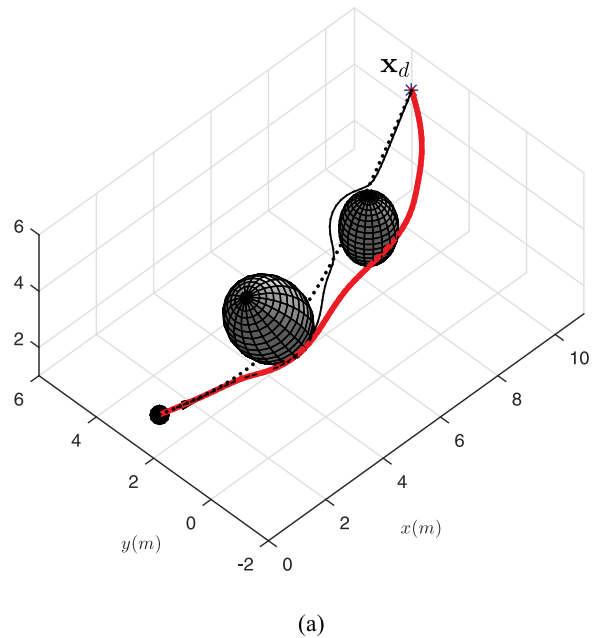


Fig. 9. Weights for the individual streamlines to avoid multiple spheroidal obstacles to produce the resulting trajectory using (11). The weight α_i for obstacle $i = 1, 2, 3$ as computed using (12).



The simultaneous avoidance of multiple obstacles can be clearly observed between the time periods $3 \leq t \leq 4.5$ s and $6 \leq t \leq 6.5$ s. Fig. 9 shows that during $3 \leq t \leq 4.5$ s, the avoidance of obstacles 1 and 3 is achieved by taking a weighted sum of trajectories \dot{x}_1 and \dot{x}_3 . This corresponds to the section of the trajectory in Fig. 8(b) that travels through the gap between obstacles 1 and 3.

3) *Multiple Obstacle Avoidance in the Presence of Curvature Constraints:* In this example, the effect of curvature constraints on the resulting trajectory to avoid multiple spheroidal obstacles is illustrated. Fig. 10 shows the resulting trajectories for three different scenarios given the same starting location, destination point, and obstacle locations (if applicable): 1) no obstacles are considered; 2) avoidance of obstacles is considered; and 3) the avoidance of obstacles with a maximum curvature constraint of $\kappa_{max} = 0.5 \text{ m}^{-1}$.

The scenario when no obstacles are considered is shown by the dotted line trajectory in Fig. 10. It can be observed in Fig. 10(b) that the planned trajectory collides with both of the spheroidal obstacles. The thin black line represents the planned trajectory from (11) to avoid the obstacles with the speed

Fig. 10. Avoidance of multiple obstacles subject to no constraints (thin black line) and maximum curvature constraint $\kappa_{max} = 0.5 \text{ m}^{-1}$ (thick red line). The trajectory with only one source and one sink, not considering obstacles, is shown by the dotted line. (a) Three-dimensional view. (b) xy view.

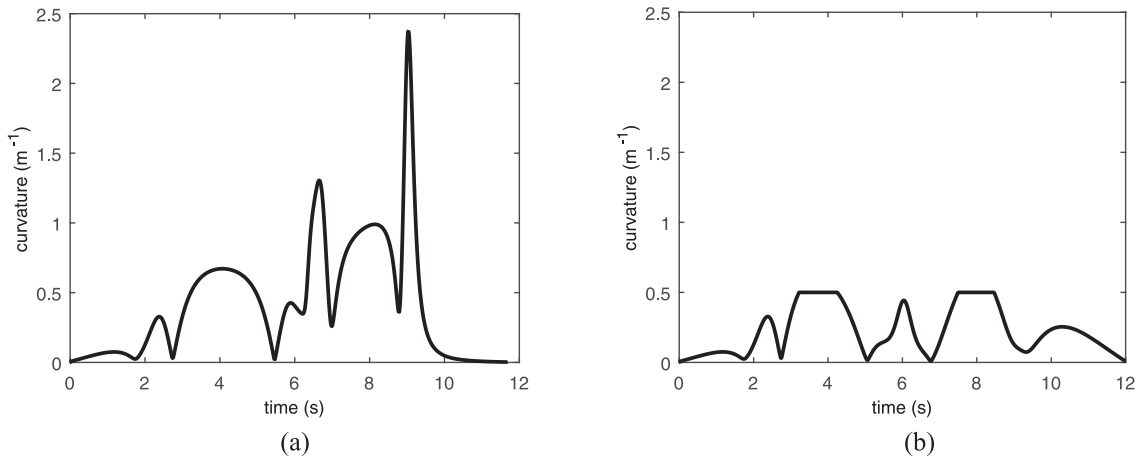


Fig. 11. Curvature for the trajectories shown in the example of Fig. 10. (a) No curvature constraint. (b) Maximum curvature constraint $\kappa_{\max} = 0.5 \text{ m}^{-1}$.

constraint $\|\mathbf{v}\| = 1 \text{ m/s}$ and no maximum curvature constraint. It can be observed that as in the previous example, the motion planner produces a trajectory that travels in between the two obstacles. However, when a maximum curvature constraint of $\kappa_{\max} = 0.5 \text{ m}^{-1}$ is applied, where the trajectory is shown by the thick red line, the planned path drastically changes to satisfy this constraint. Fig. 11 shows the curvature profiles for the trajectories with no curvature constraints and when $\kappa_{\max} = 0.5 \text{ m}^{-1}$.

From the curvature profiles, it can be seen that traveling in between the two obstacles to reach the destination requires large curvature to perform the sharper turns. In comparison, a constraint of $\kappa_{\max} = 0.5 \text{ m}^{-1}$ restricts the turning capabilities of the robot. As a result, the trajectory path remains on the left of both obstacles in order to satisfy the curvature constraints. Fig. 11(b) shows that the planned trajectory indeed satisfies the maximum curvature constraints. This example serves to illustrate that the proposed motion planner is able to plan different trajectory paths to avoid obstacles when different constraints are present. Finally, as discussed in Section III-C, the maximum curvature constraint κ_{\max} may result in no feasible trajectory. For example, this occurs when κ_{\max} is lowered to a value of $\kappa_{\max} = 0.3 \text{ m}^{-1}$.

B. Discussion

As demonstrated in the formulation of the motion planner and the examples, the proposed approach has a unique set of advantages. Compared with other 3-D motion planning approaches, the proposed method is not only computationally efficient to generate trajectories for nonholonomic robots, but also intuitively allows the inclusion of velocity level kinematic constraints. The ability to adjust characteristics of the trajectory by controlling the source and sink strengths allows kinematic constraints to be incorporated.

The computational efficiency of 2-D fluid flow motion planners [19]–[22] is maintained since closed-form expressions of the trajectory velocity can be derived using (5), (9), and (11). As a result, the computational efficiency of the method to gen-

erate the next trajectory velocity has a constant time complexity $O(1)$ with respect to the path resolution and is linear $O(n)$ to the number of obstacles as shown in (11).

APF approaches are an interesting topic that has been investigated in the study of motion planning due to its intuitive formulation to generate smooth paths and closed-form expressions of the trajectory velocity. Compared with existing panel APF approaches that have a time complexity of $O(n^3)$ for increasing number of obstacles, the proposed method is able to handle environments with more obstacles with greater efficiency. Furthermore, existing APF approaches have not considered the satisfaction of kinematic constraints in 3-D. The primary drawback of the proposed method is the limited range of obstacle shapes that it can avoid. However, as proposed in [25] and [26], complex geometries can typically be encapsulated by spheroid shapes.

V. CONCLUSION

A simple and efficient motion planning method for nonholonomic robots in 3-D using a fluid flow model has been proposed. This technique extends from conventional 2-D fluid flow motion planners. Furthermore, the proposed approach allows the avoidance of multiple spheroidal obstacles. It was demonstrated that through the appropriate selection of the strengths for the source and sink elements within the model, speed and curvature constraints on the trajectory can be satisfied. Compared with previous APF approaches, the proposed method intuitively considers kinematic constraints and handle obstacle avoidance more efficiently in 3-D. Future work will focus on the extension of this method to avoid a wider range of obstacle shapes.

REFERENCES

- [1] T. R. Wan, W. Tang, and H. Chen, "A real-time 3D motion planning and simulation scheme for nonholonomic systems," *Simul. Modell. Pract. Theory*, vol. 19, no. 4, pp. 423–439, 2011.
- [2] G. Cruz and P. Encarnacao, "Obstacle avoidance for unmanned aerial vehicles," *J. Intell. Robot. Syst.*, vol. 65, pp. 203–217, 2012.
- [3] H. Adeli, M. Tabrizi, A. Mazloomian, E. Hajipour, and M. Jahed, "Path planning for mobile robots using iterative artificial potential field method," *Int. J. Comput. Sci. Issue*, vol. 8, pp. 28–32, 2011.

- [4] J. Guldner, V. I. Utkin, and H. Hashimoto, "Robot obstacle avoidance in n-dimensional space using planar harmonic artificial potential fields," *J. Dyn. Syst. Meas. Control*, vol. 119, pp. 160–166, 1997.
- [5] J. M. Grasmeyer and M. Keennon, "Development of the black widow micro air vehicle," *Prog. Aeronaut. Astronaut.*, vol. 195, 2001, pp. 519–536.
- [6] R. Teo, J. S. Jang, and C. J. Tomlin, "Automated multiple UAV flight—The Stanford DragonFly UAV Program," in *Proc. IEEE Conf. Dec. Cont.*, 2004, pp. 4268–4273.
- [7] L. Filippis, G. Guglieri, and F. Quagliotti, "Path planning strategies for UAVs in 3D environments," *J. Intell. Robot. Syst.*, vol. 65, pp. 247–264, 2012.
- [8] M. Hwangbo, J. Kuffner, and T. Kanade, "Efficient two-phase 3D motion planning for small fixed-wing UAVs," in *Proc. IEEE Int. Conf. Robot. Autom.*, 2007, pp. 1035–1041.
- [9] S. Bortoff, "Path planning for UAVs," in *Proc. Am. Cont. Conf.*, 1998, vol. 1, pp. 364–368.
- [10] S. Karaman and E. Frazzoli, "Optimal kinodynamic motion planning using incremental sampling-based methods," in *Proc. IEEE Conf. Decision Control*, 2010, vol. 7, pp. 7681–7687.
- [11] A. Scheur and T. Fraichard, "Planning continuous-curvature paths for car-like vehicles," in *Proc. IEEE/RSJ Int. Conf. Intell. Robot. Sys.*, 1996, vol. 3, pp. 1304–1311.
- [12] J. Sampaio, "Planning 3D well trajectories using spline-in-tension functions," *J. Energy Res. Technol.*, vol. 129, pp. 289–299, 2007.
- [13] S. Khansari Zadeh and A. Billard, "A dynamical system approach to realtime obstacle avoidance," *Auton. Robots*, vol. 32, pp. 433–454, 2012.
- [14] A. Berry, J. Howitt, D.-W. Gu, and I. Postlethwaite, "A continuous local motion planning framework for unmanned vehicles in complex environments," *J. Intell. Robot Syst.*, vol. 66, pp. 477–494, 2012.
- [15] O. Khatib, "Real-time obstacle avoidance for manipulators and mobile robots," *Int. J. Robot. Res.*, vol. 5, pp. 90–98, 1986.
- [16] R. Tilove, "Local obstacle avoidance for mobile robots based on the method of artificial potentials," in *Proc. IEEE Int. Conf. Robot. Autom.*, 1990, vol. 2, pp. 566–571.
- [17] J.-O. Kim and P. K. Khosla, "Real-time obstacle avoidance using harmonic potential functions," *IEEE Trans. Robot. Autom.*, vol. 8, pp. 338–349, Jun. 1992.
- [18] Y. Zhang and K. P. Valavanis, "A 3-D potential panel method for robot motion planning," *Robotica*, vol. 15, pp. 421–434, 1997.
- [19] S. Waydo and R. M. Murray, "Vehicle motion planning using stream functions," in *Proc. IEEE Int. Conf. Robot. Autom.*, 2003, vol. 2, pp. 2484–2491.
- [20] Z. Li and T. Bui, "Robot path planning using fluid model," *J. Intell. Robot. Syst.*, vol. 21, pp. 29–50, 1998.
- [21] S. Sugiyama, J. Yamada, and T. Yoshikawa, "Path planning of a mobile robot for avoiding obstacles with improved velocity control by using the hydrodynamic potential," in *Proc. IEEE Int. Conf. Robot. Autom.*, 2010, pp. 1421–26.
- [22] T. Owen, R. Hillier, and D. Lau, "Smooth path planning around elliptical obstacles using potential flow for non-holonomic robots," in *RoboCup 2011: Robot Soccer World Cup XV*. New York, NY, USA: Springer, 2011.
- [23] P. Weiss, "On hydrodynamical images. arbitrary irrotational flow disturbed by a sphere," *Math. Proc. Cambridge Philos. Soc.*, vol. 40, pp. 259–261, 1944.
- [24] R. D. Almeda and H. R. Malonek, "On a higher dimensional analogue of the Joukowski transformation," in *Proc. Am. Inst. Phys. Conf.*, 2008, vol. 1048, pp. 630–633.
- [25] V. Matiukas and D. Miniotas, "Point cloud merging for complete 3D surface reconstruction," *Electron. Electr. Eng.*, vol. 113, pp. 73–76, 2011.
- [26] N. Vandapel, J. Kuffner, and O. Amidi, "Planning 3-D path networks in unstructured environments," in *Proc. IEEE Int. Conf. Robot. Autom.*, 2005, pp. 4624–4629.
- [27] D. Lau, J. Eden, and D. Oetomo, "Motion planning of a planar 3R manipulator utilising fluid flow trajectory generation," presented at the Australasian Conf. Robot. Autom., Wellington, New Zealand, 2012.
- [28] S. Axler, P. Bourdon, and R. Wade, *Harmonic Function Theory*. New York, NY, USA: Springer Science & Business Media, 2001, vol. 137.